

# Quantitative Assessment of Carrier Density by Cathodoluminescence (2): GaAs nanowires

Hung-Ling Chen,<sup>1</sup> Romaric De Lépinau,<sup>1,2</sup> Andrea Scaccabarozzi,<sup>1</sup> Fabrice Oehler,<sup>1</sup> Jean-Christophe Harmand,<sup>1</sup> Andrea Cattoni,<sup>1</sup> and Stéphane Collin<sup>1,2</sup>

<sup>1</sup>*Centre for Nanoscience and Nanotechnology (C2N), CNRS, Université Paris-Sud/Paris-Saclay, 91120 Palaiseau, France*

<sup>2</sup>*Institut Photovoltaïque d’Ile-de-France (IPVF), 91120 Palaiseau, France*

(Dated: May 16, 2022)

Precise control of doping in single nanowires (NWs) is essential for the development of NW-based devices. Here, we investigate a series of MBE-grown GaAs NWs with Be (p-type) and Si (n-type) doping using high-resolution cathodoluminescence (CL) mapping at low- and room-temperature. CL spectra are analyzed selectively in different regions of the NWs. Room-temperature luminescence is fitted with the generalized Planck’s law and an absorption model, and the bandgap and band tail width are extracted. For Be-doped GaAs NWs, the bandgap narrowing provides a quantitative determination of the hole concentration ranging from about  $1 \times 10^{18}$  to  $2 \times 10^{19} \text{ cm}^{-3}$ , in good agreement with the targeted doping levels. For Si-doped GaAs NWs, the electron Fermi level and the full-width at half maximum of low-temperature CL spectra are used to assess the electron concentration to approximately  $3 \times 10^{17}$  to  $6 \times 10^{17} \text{ cm}^{-3}$ . These findings confirm the difficulty to reach highly-doped n-type GaAs NWs, may be due to doping compensation. Notably, signatures of high concentration ( $5\text{--}9 \times 10^{18} \text{ cm}^{-3}$ ) at the very top of NWs are unveiled.

## I. INTRODUCTION

Semiconductor nanostructures are widely investigated in fundamental research and for device applications. In particular, III-V nanowires (NWs) have attracted a growing interest for the development of optoelectronic devices such as laser [1–3], light-emitting diodes [4–6], photodetectors [7, 8] and solar cells [9–12]. For instance, the ability to grow defect-free III-V NWs on silicon (Si) allows for the direct growth of III-V/Si tandem solar cells [13]. Doping is a key element for optimal operation of the devices like ohmic contacts [14] or efficient carrier collection [15]. Owing to the small dimensions of NWs, the realization of radial or axial p-n junctions requires a very tight control of the doping conditions during the epitaxial growth. However, characterization of carrier densities at the sub-micrometer scale remains challenging.

Field effect measurements [16, 17] and Hall effect measurements [18, 19] have been used to assess the transport properties of single NWs, but they require the fabrication of nanoscale electrical contacts, which is technically difficult. Multi probes in an electron microscope have been used to examine the charge carrier depletion and doping profile along NWs [20, 21]. Off-axis electron holography employs electron interference to measure the electrical potential in a thin specimen [22], and have been used to reveal doping inhomogeneities in core-shell GaAs NWs [23]. Time-of-flight secondary ion mass spectroscopy (SIMS) [24] and atom probe tomography (APT) [25] can also be used to measure the density of atom impurities, but carrier concentration may be hindered by electrical deactivation or dopant compensation. Alternatively, optical methods provide rapid and contactless analysis of samples without additional processing step. For instance, the collective oscillation of free carri-

ers can be excited and measured in the terahertz domain, but the low spatial resolution limits this technique to the investigation of NW ensembles [26]. Raman spectroscopy allow to probe the carrier densities through longitudinal optical (LO) phonon-plasmon interactions [27, 28]. Light scattering from local vibrational modes of the Si atom in GaAs lattice may also indicate whether Si dopants occupy As sites (p-type doping) [29, 30] or Ga sites (n-type doping) [31]. Photoluminescence (PL) is widely used and the Burstein-Moss shift was observed in n-InP [32], n-GaAs [33] and n-InAs [34] NWs. However, these optical techniques do not provide the spatial resolution required to study inhomogeneous NWs.

Here, we use cathodoluminescence (CL) mapping as a rapid, contactless measurement method of the carrier density in single NWs. The high spatial resolution of this technique allows to distinguish different regions of a single NW. It is used to eliminate faulty regions and to study variations of the carrier concentration in well-controlled homogeneous regions. In a previous work, we have demonstrated the quantitative analysis of electron concentration in Si-doped GaAs NWs [35], and the luminescence analysis method has been further validated on a series of p-type and n-type GaAs planar reference thin films [36]. Here, we extend this work to a series of Be-doped (core and shell) and Si-doped (shell) GaAs NWs grown under different conditions. We assess quantitatively the carrier densities of both p-type and n-type NWs, either by fitting room-temperature (RT) CL spectra with the generalized Planck’s law and an absorption model, or with the full-width at half maximum (FWHM) of low-temperature (LT) CL spectra. We discuss the agreement (p-doped) and disagreement (n-doped) with the target doping levels. In GaAs:Si NWs, we also unveil signatures of doping compensation that limits the carrier concentration in the shell, and of high concentrations in

the top regions.

## II. EXPERIMENTAL DETAILS

NWs were grown on a patterned Si(111) substrate by molecular beam epitaxy (MBE). A SiO<sub>2</sub> film (thickness ~25 nm) was deposited by plasma-enhanced chemical vapor deposition (PECVD). It is used as a mask for the selective growth of NWs. Openings were fabricated using electron-beam lithography in a polymethyl methacrylate (PMMA) resist. They consist in a hexagonal array of holes (diameter ~20 nm) with a pitch of 500 nm or 1 μm. The holes were transferred to the SiO<sub>2</sub> mask by reactive-ion etching (RIE) with SF<sub>6</sub>/CHF<sub>3</sub> gases, followed by a wet chemical etching in dilute HF:H<sub>2</sub>O (1:100) to remove the last nanometers of SiO<sub>2</sub> before loading the substrate into the MBE chamber for degassing in ultra-high vacuum.

The MBE growth was performed in a Riber Compact 32 system. The NW growth sequences and the angles of molecular beams are depicted in Fig. 1. Ga was supplied using a standard effusion cell. It first results in localized liquid Ga droplets above the mask openings. Arsenic was then supplied by a valved cracker producing As<sub>4</sub> and resulted in the NW growth via the self-catalyzed vapor-liquid-solid (VLS) method. The VLS growth was conducted at 610°C. After the VLS growth, Ga droplets were crystallized by closing the Ga shutter and increasing the As flux to roughly twice the previous value at a substrate temperature of about 500°C. We observed a zincblende GaAs crystal structure along most of the NWs, except in the NW tips (~30% of the total length, see for example CL maps of core-1 and core-2 in Fig. 4) which correspond to the droplet crystallization growth.

For two samples (core-1 and core-2), Be dopants were provided during the VLS growth and an AlGaAs passivation shell (thickness ~13 nm) was grown after the droplet crystallization. For the others (shell-1 to shell-5), the NW cores were not intentionally doped, and the doped shells were grown upon the sidewall facets of {110} family in the conventional vapor-solid (VS) mode with Be (p-type) or Si (n-type) dopants. Detailed growth parameters are given in Table I, including the growth temperature and the V-to-III beam equivalent pressure (BEP) ratio used for growing the doped core or shell.

The total length and diameter of NWs are measured from scanning electron microscope (SEM) images and averaged over several NWs of the same sample. Despite the hexagonal shape of NWs, the NW diameter is referred to the diameter of an equivalent cylinder with a cross-section of equal surface. The shell thickness is obtained by subtracting the total diameter to the typical diameter of NW core only (102±2 nm). The flux of Be- and Si-dopants was previously calibrated on GaAs(001) thin films. For core-1 and core-2, the theoretical doping concentration is calculated as the dopant flux divided by the NW growth rate (the crystallization growth at the tips

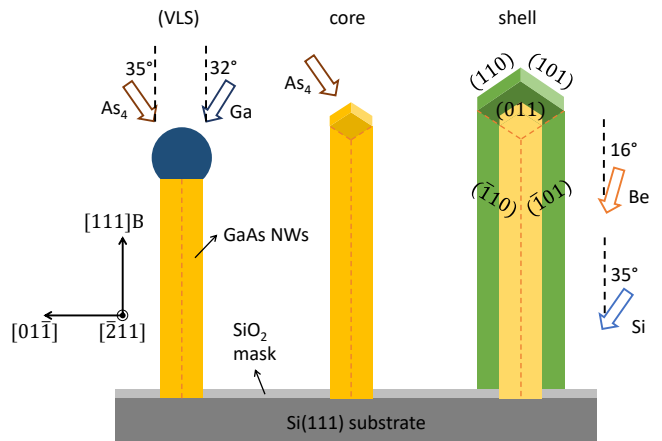


FIG. 1. Overview of the NW growth sequences. NW cores are grown using the vapor-liquid-solid (VLS) method on a Si(111) substrate patterned with a SiO<sub>2</sub> mask. Ga liquid droplets act as a catalyst of the MBE growth. They are crystallized at the end of the VLS growth. Subsequently, shell growth can be conducted (vapor-solid, VS growth) for surface passivation or to create a core-shell junction. The incident angles of molecular beams with respect to the substrate normal are indicated.

is excluded). For shell-1 to shell-5, the theoretical doping concentration is obtained similarly but taking into account the projection of the dopant flux to the vertical sidewalls and the rotation symmetry of the shell growth.

After growth, NWs were dispersed on a Si substrate. CL measurements were performed in an Attolight Chronos quantitative cathodoluminescence microscope. The e-beam acceleration voltage is 6 kV and the impinging current is 0.3–0.7 nA. Luminescence is collected by an achromatic reflective objective (NA: 0.72) and analyzed with a Horiba iHR320 monochromator (grating: 150 grooves/mm) and an Andor Newton Si CCD camera (1024×256 pixels, pixel width 26 μm, spectral dispersion: 0.53 nm per pixel). Luminescence spectra were corrected for the diffraction efficiency of the grating and the sensitivity of the CCD camera.

## III. EFFECT OF SURFACE DEPLETION AND BAND BENDING

For core-doped samples, an AlGaAs passivation shell was grown to increase the radiative efficiency of GaAs core, because thin GaAs NWs (diameter < 130 nm) without passivation suffer from severe Fermi level pinning [37]. For shell-doped samples, a relatively thick shell allowed luminescence signal to be recorded without additional surface passivation. However, the effect of surface depletion and the junction formed with the undoped core may still influence the radiative process and are discussed in the following.

Fig. 2(a) shows the GaAs surface depletion width as a

TABLE I. Description of doped GaAs NW samples. Growth temperature and V/III BEP ratio are given. NW length, diameter and shell thickness are obtained by examining SEM images (mean value  $\pm$  standard deviation). Growth rate refers to the elongation of the NW length (core doping) or the expansion of the shell thickness (shell doping) per unit of time. Dopant flux was calibrated using GaAs reference thin films and is given with respect to the substrate normal. Theoretical doping concentrations are deduced from the dopant flux and the NW growth rate.

sample	growth T. °C	V/III ratio	length $\mu\text{m}$	diameter nm	shell thick. nm	growth rate $\text{\AA}/\text{s}$	dopant atoms/(s $\cdot\text{cm}^2$ )	th. doping conc. $\text{cm}^{-3}$
core-1 (Be)	610	10	2.45 $\pm$ 0.11	189 $\pm$ 13		14.3 $\pm$ 0.7	$1.5 \times 10^{11}$	(1.0 $\pm$ 0.1) $10^{18}$
core-2 (Be)	610	10	1.85 $\pm$ 0.12	182 $\pm$ 12		10.8 $\pm$ 0.7	$8.8 \times 10^{11}$	(8.1 $\pm$ 0.6) $10^{18}$
shell-1 (Be)	550	129	2.00 $\pm$ 0.12	236 $\pm$ 8	67 $\pm$ 4	0.19 $\pm$ 0.02	$2.1 \times 10^{10}$	(1.0 $\pm$ 0.2) $10^{18}$
shell-2 (Be)	550	129	1.03 $\pm$ 0.04	282 $\pm$ 16	90 $\pm$ 8	0.25 $\pm$ 0.03	$1.5 \times 10^{11}$	(5.4 $\pm$ 0.8) $10^{18}$
shell-3 (Be)	550	129	1.99 $\pm$ 0.10	334 $\pm$ 42	116 $\pm$ 21	0.32 $\pm$ 0.06	$8.8 \times 10^{11}$	(2.5 $\pm$ 0.6) $10^{19}$
shell-4 (Si)	450	153	2.06 $\pm$ 0.10	292 $\pm$ 14	95 $\pm$ 7	0.26 $\pm$ 0.03	$4.6 \times 10^{10}$	(3.9 $\pm$ 0.4) $10^{18}$
shell-5 (Si)	475	117	2.15 $\pm$ 0.06	285 $\pm$ 22	91 $\pm$ 11	0.19 $\pm$ 0.03	$5.5 \times 10^{10}$	(6.4 $\pm$ 1.2) $10^{18}$

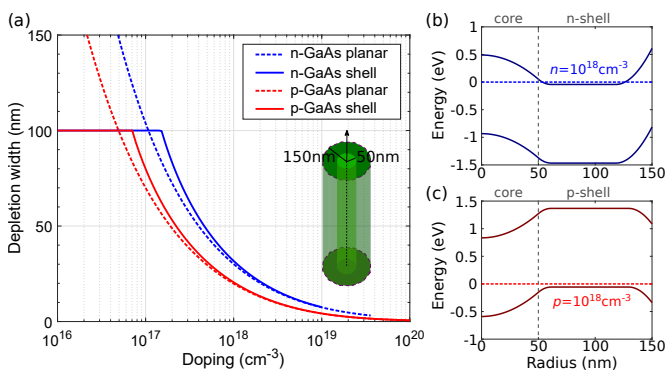


FIG. 2. (a) Calculation of the surface depletion width as a function of the doping concentration for p-GaAs (red) and n-GaAs (blue). Dashed lines correspond to bulk planar GaAs with a density of surface states  $D_s = 10^{13} \text{ cm}^{-2} \text{ eV}^{-1}$  and a fixed charge neutrality level at 0.53 eV above the valence band maximum. Solid lines represent the shell width of the depletion region for GaAs NWs (radius 150 nm) with the same surface properties. (b,c) Band diagram along the NW radius for (b) n-doped and (c) p-doped GaAs NW.

function of the doping concentration for thin films and for NWs modeled as infinite cylinders of 150 nm radius with uniform doping. It is calculated using the electrostatic model of Ref. [38] with the charge neutrality level of GaAs taken to be 0.53 V above the valence band [39], and a density of surface states of  $10^{13} \text{ cm}^{-2} \text{ eV}^{-1}$  corresponding to GaAs with native oxide [40]. NWs behave as thin films at high doping levels, but present larger surface depletion width at low doping concentrations. The NWs are totally depleted below a certain concentration limit. Under e-beam excitation, the separation of quasi-Fermi levels decreases toward the surface due to surface recombination. Hence, the CL contribution from the surface depletion region should be significantly lower than that from below the surface depletion region.

In the case where an unintentionally doped core is present, the doped shell may be partly depleted near the

core-shell interface. This is illustrated in Fig. 2(b,c) for n-doped and p-doped shell. Free carriers can diffuse to the core, leading to band bending (bend up for n-shell and bend down for p-shell). Because of high doping levels in the shell and the small volume of the core, the effect of free carrier depletion in the shell should be negligible. Under e-beam excitation, most of the excess carriers are generated in the shell (depth of the generation volume  $\sim 70$  nm with a cut-off defined as 80% of the maximum energy [35]). In addition, carriers generated in the core would be separated due to the internal field, resulting in low CL contribution from the core. CL measurements on shell-doped samples should mainly probe the quasi-neutral region of doped shells.

#### IV. BE-DOPED GAAS NANOWIRES

The mechanism of Be incorporation in MBE-grown GaAs NWs by the VLS method is still unclear, due to the complexity introduced by the nanoscale liquid Ga droplets and the difficulty of doping characterization for single NWs. Early studies used electrical conductivity measurements along NWs and showed that Be impurities incorporate dominantly through the parasitic side-wall growth in the VS mode [41]. Recently, Be incorporation through the three (112)A truncated facets at the liquid-solid interface was inferred using electron holography to evidence a remarkable three-fold symmetry of the electrical potential [23]. On the other hand, homogeneous incorporation was observed using the reconstruction with atom probe tomography [42]. In our experiments, we observed rather homogeneous CL mapping for Be-doped NW core, suggesting homogeneous incorporation in our growth conditions. For Be-doped NW shells, the situation should be similar to usual thin film growth and efficient doping incorporation was found using a high V/III ratio [43].

Fig. 3 shows SEM images of as-grown NWs on Si substrates for the five Be-doped samples. Two of them are

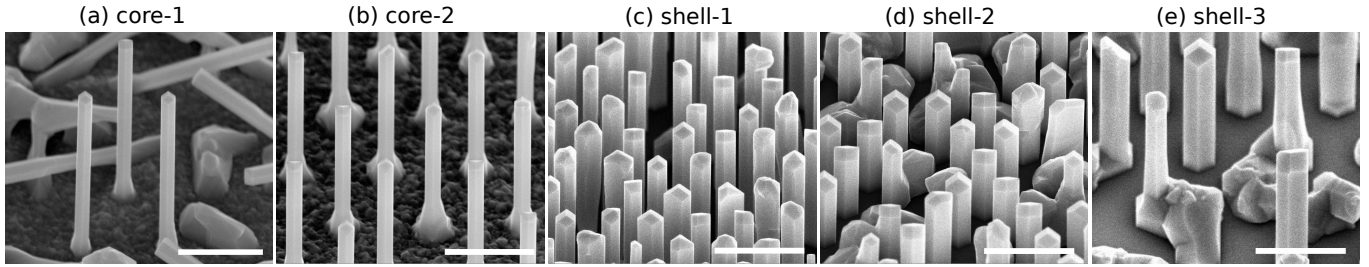


FIG. 3. SEM images of GaAs:Be NWs on Si(111) substrates with a 45 degree sample tilt. (a,b) NWs with direct Be doping during the VLS growth. After crystallization of the Ga droplets, an AlGaAs shell was grown for surface passivation. (c,d,e) NW structures containing undoped GaAs core and Be-doped shell without additional surface passivation. Scale bars are  $1 \mu\text{m}$ .

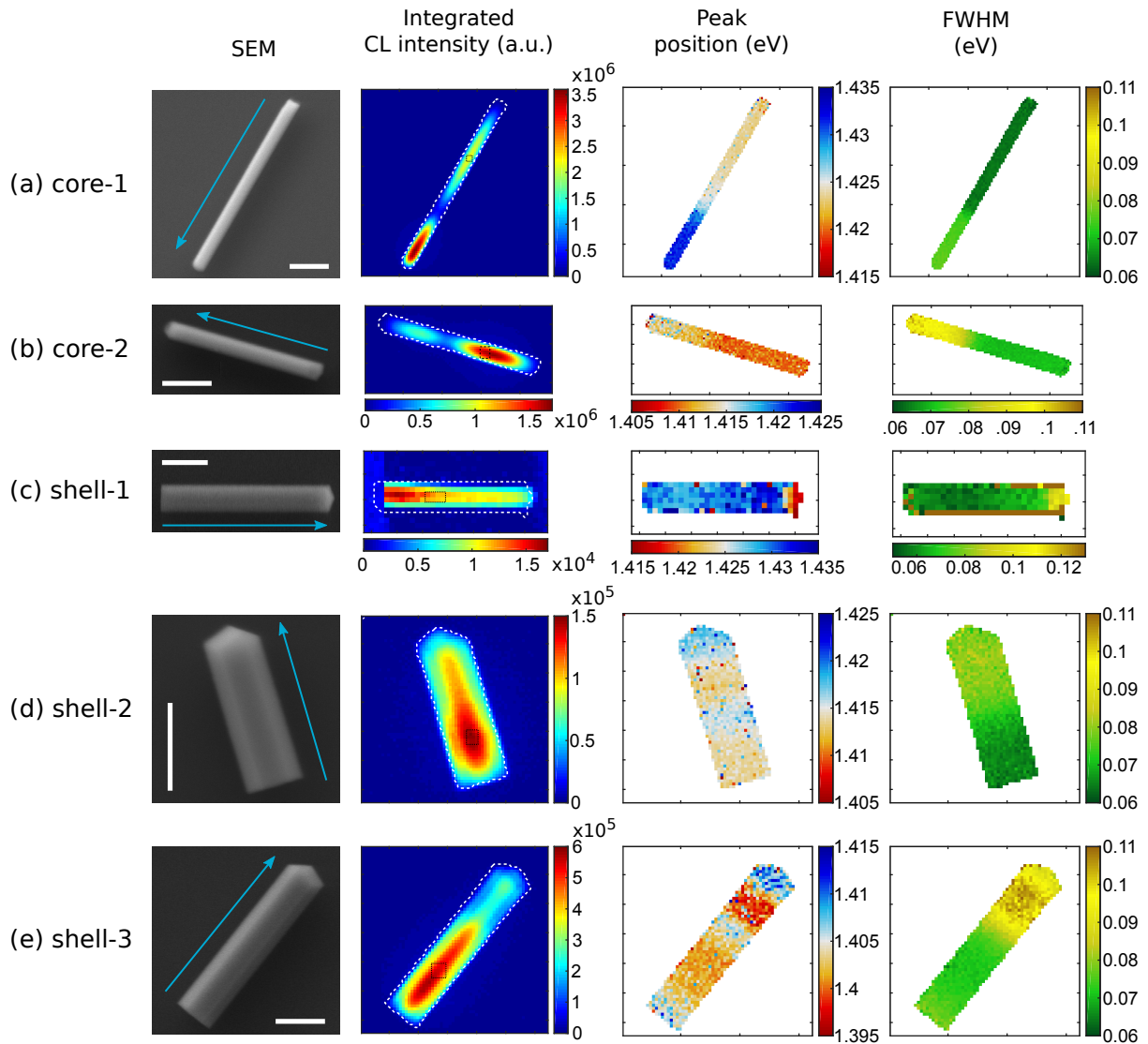


FIG. 4. Room-temperature CL maps of Be-doped GaAs NWs. For each CL measurement, SEM image of the NW and maps of the integrated CL intensity, the CL peak position and the FWHM are shown. Arrows indicate the growth direction from the bottom to the top of the NWs. Scale bars are 500 nm.

TABLE II. CL characteristics of GaAs:Be NW samples. Peak position and FWHM are typical for CL spectra extracted from the middle homogeneous part of the NWs. The bandgap  $E_g$  and Urbach tail  $\gamma$  are determined from the fit of CL spectra with the generalized Planck's law. Experimental hole concentrations are obtained from the BGN values.

sample	peak eV	FWHM eV	$E_g$ eV	$\gamma$ meV	exp. hole conc. $\text{cm}^{-3}$
core-1	1.423	0.065	1.404	13	$1.9 \times 10^{18}$
core-2	1.411	0.073	1.387	15	$1.2 \times 10^{19}$
shell-1	1.429	0.060	1.412	12	$< 1 \times 10^{18}$
shell-2	1.413	0.070	1.394	15	$6.6 \times 10^{18}$
shell-3	1.401	0.073	1.381	15	$1.9 \times 10^{19}$

doped during the VLS growth (core-1 and -2), three are doped during the VS growth of NW shells (shell-1, -2 and -3). The statistics of the NW geometry are given in Table I. The growth parameters were kept identical except for the flux of Be dopant, but slight variations of the NW geometry and morphology are still observed. Be dopant is believed to have a surfactant effect which may cause irregular morphology and kinked NWs at high Be concentration [42]. In our samples, regular morphology was obtained along most of the NW length, and eventual inhomogeneity at the top can be resolved with CL mapping.

Fig. 4 shows room-temperature (RT) CL measurements of Be-doped NWs. Every NW was measured with the same condition for electron excitation and luminescence collection, so their integrated CL intensities can be quantitatively compared. It allows for a direct comparison of the radiative efficiencies between samples. The color scales for the CL peak position and full-width at half maximum (FWHM) are adapted for each sample to visualize variations inside single NWs. For core-doped samples, two distinct regions with different CL characteristics are visible. The top of the NWs exhibits blueshifted luminescence peaks with a significant broadening. It may be due to the crystal phase mixing occurring during the droplet crystallization [44, 45]. Here, we focus on the homogeneous region in the middle of the NWs in order to assess and compare the carrier density between samples. We have checked by transmission electron microscope that this region is made of pure zincblende crystal phase (not shown).

Average CL spectra are extracted from the homogeneous regions delimited by the small rectangles shown in Fig. 4 (integrated CL intensity maps). They are plotted in Fig. 5(a) and can be compared quantitatively. The higher intensities are obtained with the core-doped samples, demonstrating the effective passivation effect of AlGaAs shells. The intensities for the shell-doped samples increase with the doping levels. In particular, the lowest doped NW (shell-1) exhibits a very low luminescence intensity due to a thinner shell and a larger surface deple-

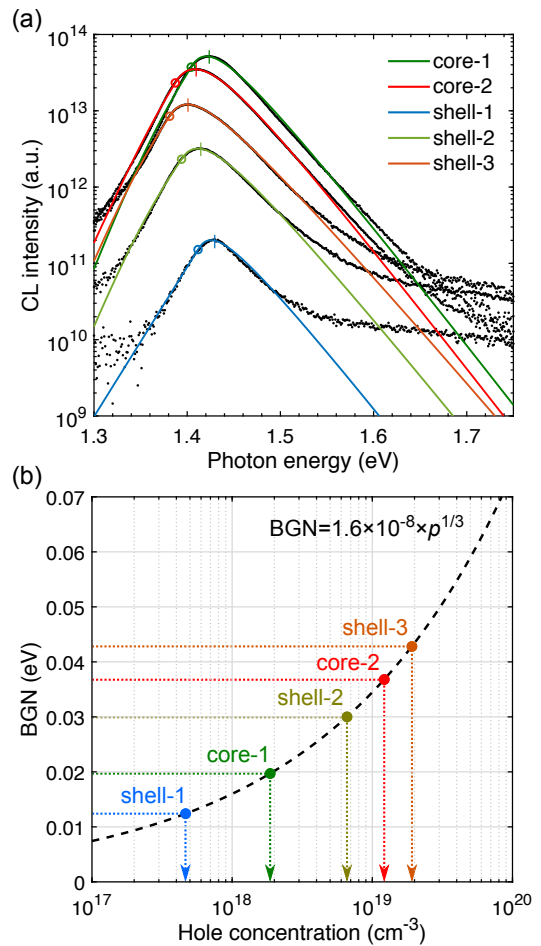


FIG. 5. (a) CL spectra of Be-doped GaAs NWs (black dots) and fits (colored lines). CL spectra are extracted from the middle homogeneous part of the CL maps (rectangles in Fig. 4). Vertical bars mark the CL peak positions, and open circles mark the bandgap deduced from the fit of the generalized Planck's law. (b) Empirical relation used to access the hole concentration from the BGN values, from Ref. [36, 46].

tion width. Redshift and broadening of CL spectra are consistent with an increased p-type doping, as expected from the Be flux (Table I).

CL spectra are fitted using the generalized Planck's law and a parabolic absorption model convoluted with an Urbach tail, following the method described in Ref. [36]. Due to the small size of the NWs, we neglect the reabsorption effect so that the absorptivity is approximated by the absorption coefficient  $\alpha(\hbar\omega)$  [47]. The results are plotted in Fig. 5(a) (colored lines). The fitted model provides the bandgap  $E_g$  (open circles in Fig. 5(a)) and energy width of the Urbach tail  $\gamma$ . Both values depend mainly on the low-energy part of the luminescence spectra. Table II lists the Be-doped GaAs NW samples, the characteristics of CL spectra (peak energy and FWHM),  $E_g$  and  $\gamma$ . Experimental hole concentrations are deduced from the bandgap narrowing (BGN) values:  $\text{BGN} = 1.424 - E_g$  (eV), and the empirical rela-

tion of Casey and Stern [46], see Fig. 5(b). For shell-1, the BGN value is too small to give a precise assessment of the hole concentration, which is probably lower than  $1 \times 10^{18} \text{ cm}^{-3}$ .

The carrier concentrations determined by CL (Table II) are in good agreement with the expected doping levels (Table I). For core-doped samples, measurements are slightly higher than expected. This can be related to a larger cross-section of the liquid droplets than the cross-section of the NWs used to estimate the incorporation of dopants. It results in a larger amount of Be atoms captured by the liquid droplets during the VLS growth of NWs and contribute to the overall doping of the core. Be incorporation through the truncated facets may also contribute to the doping and concentrate the dopants locally in the NW core [23], leading to a larger BGN observed from CL. For shell-doped samples, the small discrepancy between the theoretical and experimental doping concentrations may be due to the uncertainty of the growth rate and complex orientation and shadowing of the impinging dopant flux. Overall, Be-doping in the core or shell of GaAs NWs can be accurately controlled through CL calibration.

## V. SI-DOPED GAAS NANOWIRES

Si dopant is another contentious topic in GaAs NW growth due to its amphoteric behavior. It is normally utilized as an n-type dopant for GaAs thin films with (001) surface orientation, and typical free electron concentration up to  $7 \times 10^{18} \text{ cm}^{-3}$  without dopant compensation can be achieved in MBE systems [48]. However, the higher temperature required for the VLS growth of NWs results in higher As desorption rates and thus increases the probability of Si to occupy As sites [49]. Moreover, the incorporation mechanism differs largely in the presence of a liquid phase. Indeed, Si-doped GaAs grown by liquid phase epitaxy (LPE) is mainly compensated [50]. p-type doping was observed in GaAs NWs grown by VLS [29, 51]. On the other hand, shell-doping on NW facets of  $\{110\}$  type is believed to produce n-type conductivity [31]. Here, we have grown Si-doped GaAs NW shells at low temperature ( $T < 500^\circ\text{C}$ ) to investigate the n-doping characteristics by CL mapping.

Fig. 6 shows SEM images of two samples (shell-4 and shell-5). Their growth parameters, geometry and expected [Si] concentrations in the shell are given in Table I. The presence of Si atoms during the shell growth also causes parasitic growth of GaAs crystals on the  $\text{SiO}_2$  mask. The morphology of GaAs:Si NWs is regular along most of the wire length, except at the top where twin planes, stacking faults and mixed crystal phases may be induced by the crystallization of the Ga droplets [44, 45]. For shell-4, the consumption of liquid Ga droplets was conducted at higher temperature ( $610^\circ\text{C}$ ) and lower As flux (roughly one sixth of the value used during the VLS growth) to suppress the defect formation at the tip [44].

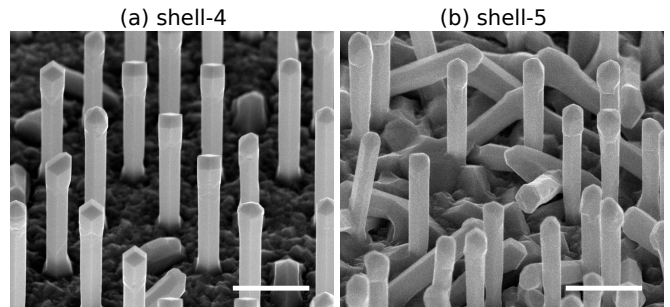


FIG. 6. SEM images of GaAs:Si NWs on Si(111) substrates with a 45 degree sample tilt. GaAs NWs are composed of undoped core and Si-doped shell without additional surface passivation. Scale bars are  $1 \mu\text{m}$ .

TABLE III. RT and LT CL characteristics of GaAs:Si NW samples. Electron Fermi levels cannot be extracted reliably from the luminescence lineshape at low concentrations. Experimental electron concentrations are assessed from the LT FWHM.

sample	RT		LT		exp. electron conc. $\text{cm}^{-3}$
	peak eV	FWHM meV	peak eV	FWHM meV	
shell-4	1.430	42	1.505	19	$3.6 \times 10^{17}$
shell-5 (A)	1.431	54	1.508	22	$4.5 \times 10^{17}$
shell-5 (C)	1.468	191	1.549	165	$9.2 \times 10^{18}$

Fig. 7 shows SEM images, RT and low-temperature (LT, 20 K) CL maps of Si-doped GaAs NWs. Shell-4 presents homogeneous CL characteristics (peak position and FWHM) along the entire wire. On the other hand, CL maps of shell-5 reveal a region (labeled B) in the top half where the CL intensity is reduced and the CL peak is redshifted. It corresponds probably to the core region grown during the droplet crystallization. The top part (labeled C) exhibits wide and blueshifted CL features, which likely corresponds to the shell growth on top of the core. The rest of the wire (bottom to middle part, labeled A) remains homogeneous.

In Fig. 8(a), we compare CL spectra extracted from shell-4 and from the bottom homogeneous region (A) and the top part (C) of shell-5. They are normalized and shifted vertically for clarity. The low-energy peak observed on RT CL spectra around 1.2–1.3 eV (dashed lines in Fig. 8(a) left) is attributed to Si-related complex defects [52–54]. The main emission peak can be fitted following the method developed in Ref. [36]. However, for the two thinner luminescence peaks of shell-4 and shell-5 (A), the electron concentration is probably below the degeneration threshold and the electron Fermi level  $E_{fc}$  cannot be deduced accurately. In contrast, the top region (C) of shell-5 exhibits a broad, blueshifted CL spectrum consistent with a high electron concentration in this region. Its main emission peak (RT) is nicely fitted with  $E_g = 1.364 \text{ eV}$ ,  $E_{fc} = 0.152 \text{ eV}$ ,  $\gamma = 29 \text{ meV}$ ,

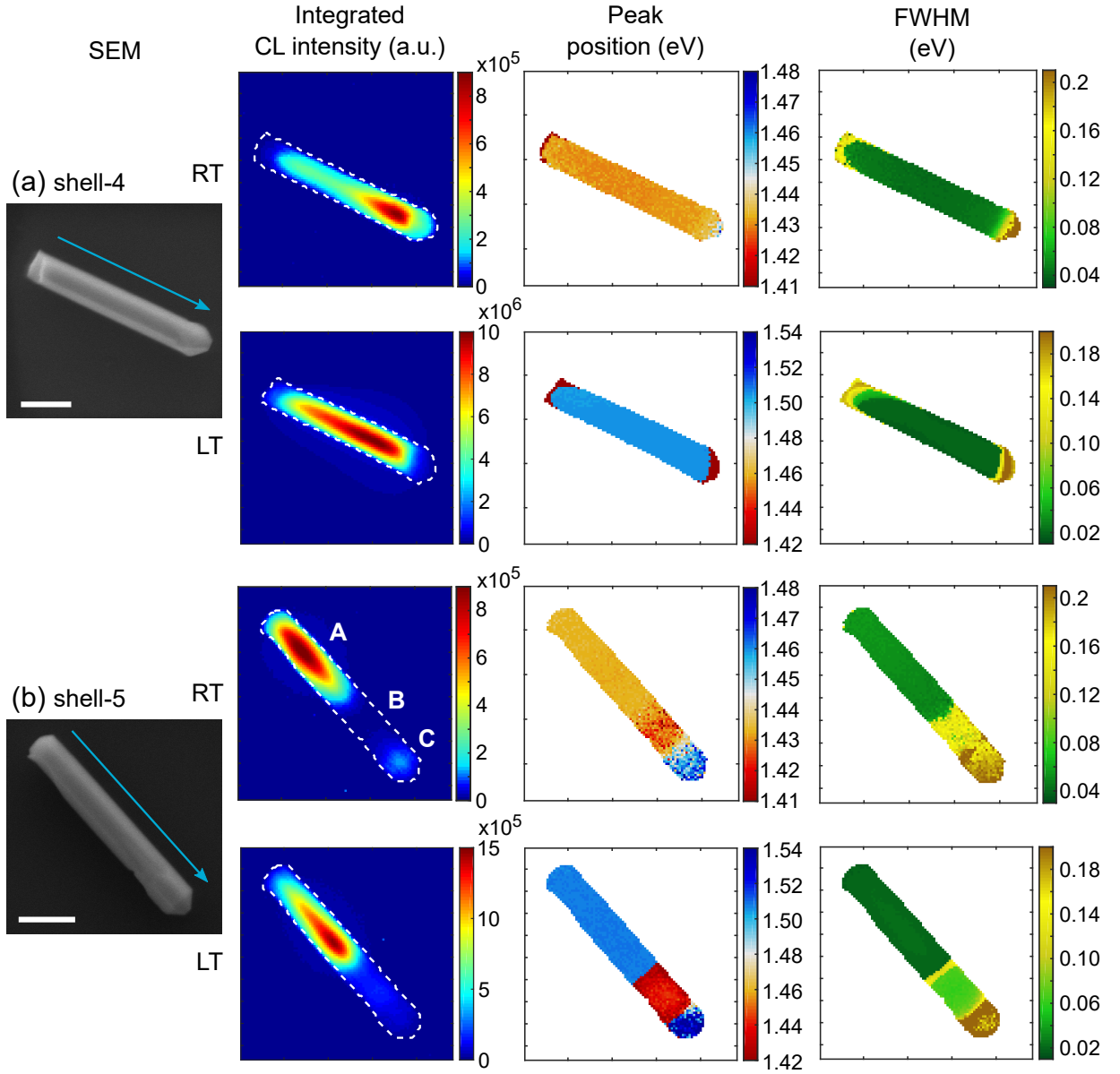


FIG. 7. SEM images, RT and LT CL maps of Si-doped GaAs NWs. For each CL measurement, maps of the integrated CL intensity, the CL peak position and the FWHM are shown. Arrows indicate the growth direction from the bottom to the top of the NWs. Scale bars are 500 nm.

and  $kT = 38$  meV. An effective higher carrier temperature is reflected from the slower decrease of the high-energy tail of the CL spectrum, as compared with the two other CL spectra. This may be related to the k-conservation in the radiative recombination of electrons above the degenerate Fermi level with holes that are not thermalized to the band edge [55]. The electron Fermi level of 152 meV corresponds to an electron concentration of  $5.1 \times 10^{18} \text{ cm}^{-3}$  [36].

To provide a more accurate assessment of the carrier density, CL measurements of the same NWs have been performed at LT. Their spectra are shown in Fig. 8(a) (right), and the luminescence characteristics (peak position and FWHM) are summarized in Table III. The

electron concentration is estimated using the LT FWHM and the empirical relation established in Ref. [36], see Fig. 8(b). We find an electron around  $4 \times 10^{17} \text{ cm}^{-3}$  for shell-4 and shell-5 (region A). For the top of shell-5 (region C), we find an electron concentration of  $9.2 \times 10^{18} \text{ cm}^{-3}$ . We note that this value may be slightly overestimated due to low-energy luminescence from the defects. Comparing with the fit of the RT CL spectrum, we infer a high carrier density of  $n = 5\text{--}9 \times 10^{18} \text{ cm}^{-3}$  at the top of shell-5.

We notice that a discrepancy of nearly one order of magnitude exists between the target doping levels (Table I) and the values deduced from CL measurements (Table III). Lowered doping efficiency in the NW shell

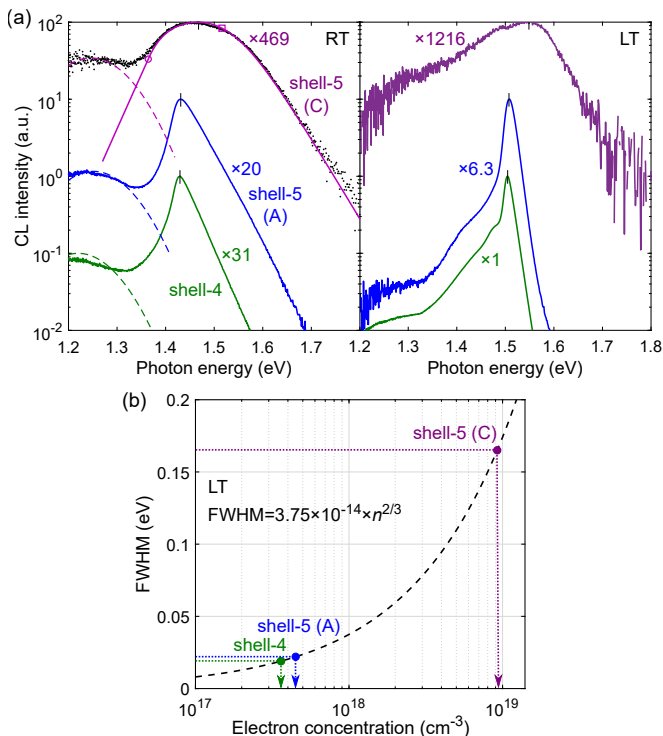


FIG. 8. (a) Room-temperature (RT, left) and low-temperature (LT, right) CL spectra of Si-doped GaAs NWs. CL spectra of shell-5 are extracted from the bottom and the top of the NW (regions A and C, respectively, see Fig. 7). The RT CL spectrum of shell-5 top (C) is fitted (solid curves) to extract the bandgap (open circles) and the electron Fermi level (open squares). (b) Empirical relation used to access the electron concentration from LT FWHM of CL spectra, from Ref. [36].

was also observed in Te-doped GaAs NWs [56]. Surface depletion [31] or Si dopant compensation due to (110) surface orientation [49] may be responsible for the ob-

served lower carrier density determined by CL. Growth issues such as inhomogeneous distribution of molecular beam or shadowing effect [57] may also hinder the incorporation of Si dopants. Further understanding of microscopic crystal growth mechanisms will be required to improve the NW growth conditions for device applications.

## VI. CONCLUSION

In this paper, we have investigated Be-doped and Si-doped GaAs NWs with different target doping concentrations. CL mapping allows to identify defective regions in single NWs and to extract spectra from homogeneous regions for further analysis. For Be-doped GaAs NWs, CL spectra progressively broaden and redshift with increasing Be flux. The bandgap narrowing is determined by fitting RT spectra with the generalized Planck's law, and used to assess quantitatively the hole concentration. It is found in very good agreement with expected doping levels. For Si-doped GaAs NWs, increased doping concentration induces a blueshift and spectral broadening related to the well-known Burstein-Moss effect. In the homogeneous region in the middle of the NWs, we infer electron concentration of  $3 \times 10^{17}$  to  $6 \times 10^{17} \text{ cm}^{-3}$  from LT FWHM of CL spectra. We also unveil signatures of higher electron concentrations ( $5\text{--}9 \times 10^{18} \text{ cm}^{-3}$ ) at the top of NWs. Luminescence from a defect band at lower energies may indicate Si dopant compensation. In conclusion, we have shown that high-resolution CL mapping and spectral analysis provide useful information for contactless assessment of carrier densities at the nanoscale. This technique can be extended to obtain insights about surface passivation, carrier lifetime and diffusion length, and the composition of a wide variety of ternary or quaternary compound semiconductors.

- [1] M. T. Hill, Y.-S. Oei, B. Smalbrugge, Y. Zhu, T. de Vries, P. J. van Veldhoven, F. W. M. van Otten, T. J. Eijkmans, J. P. Turkiewicz, H. de Waardt, E. J. Geluk, S.-H. Kwon, Y.-H. Lee, R. Nötzel, and M. K. Smit, *Nature Photonics* **1**, 589 (2007).
- [2] K. H. Li, X. Liu, Q. Wang, S. Zhao, and Z. Mi, *Nature Nanotechnology* **10**, 140 (2015).
- [3] S. W. Eaton, A. Fu, A. B. Wong, C.-Z. Ning, and P. Yang, *Nature Reviews Materials* **1**, 16028 (2016).
- [4] C. P. T. Svensson, T. Mårtensson, J. Trägårdh, C. Larsson, M. Rask, Dan Hessman, L. Samuelson, and J. Ohlsson, *Nanotechnology* **19**, 305201 (2008).
- [5] K. Tomioka, J. Motohisa, S. Hara, K. Hiruma, and T. Fukui, (2010), 10.1021/nl9041774.
- [6] N. Guan, X. Dai, A. Messanvi, H. Zhang, J. Yan, E. Gautier, C. Bougerol, F. H. Julien, C. Durand, J. Eymery, and M. Tcherynecheva, *ACS Photonics* **3**, 597 (2016).
- [7] X. Dai, S. Zhang, Z. Wang, G. Adamo, H. Liu, Y. Huang, C. Couteau, and C. Soci, *Nano Letters* **14**, 2688 (2014).
- [8] R. R. LaPierre, M. Robson, K. M. Azizur-Rahman, and P. Kuyanov, *Journal of Physics D: Applied Physics* **50**, 123001 (2017).
- [9] G. Mariani, Z. Zhou, A. Scofield, and D. L. Huffaker, *Nano Letters* **13**, 1632 (2013).
- [10] J. Wallentin, N. Anttu, D. Asoli, M. Huffman, I. Åberg, M. H. Magnusson, G. Siefer, P. Fuss-Kailuweit, F. Dimroth, B. Witzigmann, H. Q. Xu, L. Samuelson, K. Depert, and M. T. Borgström, *Science* **339**, 1057 (2013).
- [11] I. Åberg, G. Vescovi, D. Asoli, U. Naseem, J. P. Gilboy, C. Sundvall, A. Dahlgren, K. E. Svensson, N. Anttu, M. T. Björk, and L. Samuelson, *IEEE Journal of Photovoltaics* **6**, 185 (2016).
- [12] D. van Dam, N. J. J. van Hoof, Y. Cui, P. J. van Veldhoven, E. P. A. M. Bakkers, J. Gómez Rivas, and J. E. M. Haverkort, *ACS Nano* **10**, 11414 (2016).



- [13] M. Yao, S. Cong, S. Arab, N. Huang, M. L. Povinelli, S. B. Cronin, P. D. Dapkus, and C. Zhou, *Nano Letters* **15**, 7217 (2015).
- [14] L. Hüttenhofer, D. Xydias, R. B. Lewis, S. Rauwerdink, A. Tahraoui, H. Küpers, L. Geelhaar, O. Marquardt, and S. Ludwig, *Physical Review Applied* **10**, 034024 (2018).
- [15] Z. Li, Y. C. Wenas, L. Fu, S. Mokkaapati, H. H. Tan, and C. Jagadish, *IEEE Journal of Photovoltaics* **5**, 854 (2015).
- [16] Y. Cui, X. Duan, J. Hu, and C. M. Lieber, *The Journal of Physical Chemistry B* **104**, 5213 (2000).
- [17] S. A. Dayeh, D. P. R. Aplin, X. Zhou, P. K. L. Yu, E. T. Yu, and D. Wang, *Small* **3**, 326 (2006).
- [18] C. Blömers, T. Grap, M. I. Lepsa, J. Moers, S. Trelenkamp, D. Grützmacher, H. Lüth, and T. Schäpers, *Applied Physics Letters* **101**, 152106 (2012).
- [19] K. Storm, F. Halvardsson, M. Heurlin, D. Lindgren, A. Gustafsson, P. M. Wu, B. Monemar, and L. Samuelson, *Nature Nanotechnology* **7**, 718 (2012).
- [20] A. Nägelein, M. Steidl, S. Korte, B. Voigtländer, W. Prost, P. Kleinschmidt, and T. Hannappel, *Nano Research* , 1 (2018).
- [21] V. Piazza, M. Vettori, A. Ali, P. Lavenus, F. Bayle, N. Chauvin, F. H Julien, P. Regreny, G. Patriarche, A. Fave, M. Gendry, and M. Tchernycheva, *Nanoscale* (2018), 10.1039/C8NR03827A.
- [22] S. Yazdi, A. Berg, M. T. Borgström, T. Kasama, M. Beggia, L. Samuelson, and J. B. Wagner, *Small* **11**, 2687 (2015).
- [23] M. H. T. Dastjerdi, E. M. Fiordaliso, E. D. Leshchenko, A. Akhtari-Zavareh, T. Kasama, M. Aagesen, V. G. Dubrovskii, and R. R. LaPierre, *Nano Letters* **17**, 5875 (2017).
- [24] A. C. E. Chia, N. Dhindsa, J. P. Boulanger, B. A. Wood, S. S. Saini, and R. R. LaPierre, *Journal of Applied Physics* **118**, 114306 (2015).
- [25] S. Du, T. Burgess, B. Gault, Q. Gao, P. Bao, L. Li, X. Cui, W. Kong Yeoh, H. Liu, L. Yao, A. V. Ceguerra, H. Hoe Tan, C. Jagadish, S. P. Ringer, and R. Zheng, *Ultramicroscopy IFES 2012*, **132**, 186 (2013).
- [26] H. J. Joyce, J. L. Bolland, C. L. Davies, S. A. Baig, and M. B. Johnston, *Semiconductor Science and Technology* **31**, 103003 (2016).
- [27] K. Jeganathan, R. K. Debnath, R. Meijers, T. Stoica, R. Calarco, D. Grützmacher, and H. Lüth, *Journal of Applied Physics* **105**, 123707 (2009).
- [28] M. S. Mohajerani, S. Khachadorian, T. Schimpke, C. Nenstiel, J. Hartmann, J. Ledig, A. Avramescu, M. Strassburg, A. Hoffmann, and A. Waag, *Applied Physics Letters* **108**, 091112 (2016).
- [29] B. Ketterer, E. Mikheev, E. Uccelli, and A. Fontcuberta i Morral, *Applied Physics Letters* **97**, 223103 (2010).
- [30] B. Ketterer, E. Uccelli, and A. Fontcuberta i Morral, *Nanoscale* **4**, 1789 (2012).
- [31] E. Dimakis, M. Ramsteiner, A. Tahraoui, H. Riechert, and L. Geelhaar, *Nano Research* **5**, 796 (2012).
- [32] D. Lindgren, O. Hultin, M. Heurlin, K. Storm, M. T. Borgström, L. Samuelson, and Anders Gustafsson, *Nanotechnology* **26**, 045705 (2015).
- [33] S. Arab, M. Yao, C. Zhou, P. D. Dapkus, and S. B. Cronin, *Applied Physics Letters* **108**, 182106 (2016).
- [34] M. Sonner, J. Treu, K. Saller, H. Riedl, J. J. Finley, and G. Koblmüller, *Applied Physics Letters* **112**, 091904 (2018).
- [35] H.-L. Chen, C. Himwas, A. Scaccabarozzi, P. Rale, F. Oehler, A. Lemaitre, L. Lombez, J.-F. Guillemoles, M. Tchernycheva, J.-C. Harmand, A. Cattoni, and S. Collin, *Nano Letters* **17**, 6667 (2017).
- [36] H.-L. Chen, A. Scaccabarozzi, R. D. Lépinau, F. Oehler, A. Lemaitre, J.-C. Harmand, A. Cattoni, and S. Collin, submitted (2019).
- [37] O. Demichel, M. Heiss, J. Bleuse, H. Mariette, and A. Fontcuberta i Morral, *Applied Physics Letters* **97**, 201907 (2010).
- [38] A. C. E. Chia and R. R. LaPierre, *Journal of Applied Physics* **112**, 063705 (2012).
- [39] F. Gozzo, C. Coluzza, G. Margaritondo, and F. Flores, *Solid State Communications* **81**, 553 (1992).
- [40] D. E. Aspnes, *Surface Science* **132**, 406 (1983).
- [41] A. Casadei, P. Krogstrup, M. Heiss, J. A. Röhr, C. Colombo, T. Ruelle, S. Upadhyay, C. B. Sørensen, J. Nygård, and A. Fontcuberta i Morral, *Applied Physics Letters* **102**, 013117 (2013).
- [42] Y. Zhang, Z. Sun, A. M. Sanchez, M. Ramsteiner, M. Aagesen, J. Wu, D. Kim, P. Jurczak, S. Huo, L. J. Lauhon, and H. Liu, *Nano Letters* **18**, 81 (2018).
- [43] S. K. Ojha, P. K. Kasanaboina, C. Lewis Reynolds, T. A. Rawdanowicz, Y. Liu, R. M. White, and S. Iyer, *Journal of Vacuum Science & Technology B* **34**, 02L114 (2016).
- [44] M. H. T. Dastjerdi, J. P. Boulanger, P. Kuyanov, M. Aagesen, and R. R. LaPierre, *Nanotechnology* **27**, 475403 (2016).
- [45] C. Himwas, S. Collin, P. Rale, N. Chauvin, G. Patriarche, F. Oehler, F. H. Julien, L. Travers, J.-C. Harmand, and M. Tchernycheva, *Nanotechnology* **28**, 495707 (2017).
- [46] H. C. Casey and F. Stern, *Journal of Applied Physics* **47**, 631 (1976).
- [47] J.-J. Greffet, P. Bouchon, G. Brucoli, and F. m. c. Marquier, *Phys. Rev. X* **8**, 021008 (2018).
- [48] J. H. Neave, P. J. Dobson, J. J. Harris, P. Dawson, and B. A. Joyce, *Applied Physics A* **32**, 195 (1983).
- [49] E. S. Tok, J. H. Neave, M. J. Ashwin, B. A. Joyce, and T. S. Jones, *Journal of Applied Physics* **83**, 4160 (1998).
- [50] D. T. J. Hurle, *Journal of Applied Physics* **85**, 6957 (1999).
- [51] J. Dufouleur, C. Colombo, T. Garma, B. Ketterer, E. Uccelli, M. Nicotra, and A. Fontcuberta i Morral, *Nano Letters* **10**, 1734 (2010).
- [52] H. Kressel and H. Nelson, *Journal of Applied Physics* **40**, 3720 (1969).
- [53] S. Y. Chiang and G. L. Pearson, *Journal of Luminescence* **10**, 313 (1975).
- [54] L. Pavesi, N. H. Ky, J. D. Ganière, F. K. Reinhart, N. Baba-Ali, I. Harrison, B. Tuck, and M. Henini, *Journal of Applied Physics* **71**, 2225 (1992).
- [55] K. Mergenthaler, N. Anttu, N. Vainorius, M. Aghaeipour, S. Lehmann, M. T. Borgström, L. Samuelson, and M.-E. Pistol, *Nature Communications* **8**, 1634 (2017).
- [56] N. I. Goktas, E. M. Fiordaliso, and R. R. LaPierre, *Nanotechnology* **29**, 234001 (2018).
- [57] F. Oehler, A. Cattoni, A. Scaccabarozzi, G. Patriarche, F. Glas, and J.-C. Harmand, *Nano Letters* **18**, 701 (2018).